AFRL-RX-WP-TP-2010-4110

FORMULATIONS FOR RATE INDEPENDENT CYCLIC SINGLE CRYSTAL PLASTICITY (PREPRINT)

Alexander Staroselsky

Pratt & Whitney

Brice N. Cassenti

University of Connecticut

FEBRUARY 2010

AIR FORCE RESEARCH LABORATORY
MATERIALS AND MANUFACTURING DIRECTORATE
WRIGHT-PATTERSON AIR FORCE BASE, OH 45433-7750
AIR FORCE MATERIEL COMMAND
UNITED STATES AIR FORCE

REPORT DOCUMENTATION PAGE

Form Approved
OMB No. 0704-0188

1. REPORT DATE *(DD-MM-YY)*	2. REPORT TYPE	3. DATES COVERED *(From - To)*
February 2010	Journal Article Preprint	01 February 2010 – 01 February 2010

4. TITLE AND SUBTITLE
FORMULATIONS FOR RATE INDEPENDENT CYCLIC SINGLE CRYSTAL PLASTICITY (PREPRINT)

5a. CONTRACT NUMBER
In-house

5b. GRANT NUMBER

5c. PROGRAM ELEMENT NUMBER
62102F

6. AUTHOR(S)
Alexander Staroselsky (Pratt & Whitney)
Brice N. Cassenti (University of Connecticut)

5d. PROJECT NUMBER
4347

5e. TASK NUMBER
RG

5f. WORK UNIT NUMBER
M02R3000

7. PERFORMING ORGANIZATION NAME(S) AND ADDRESS(ES)

Pratt & Whitney
400 Main Street, MS 165-16
East Hartford, CT 06108

University of Connecticut
191 Auditorium Rd. U-3139
Storrs, CT 06269-3139

8. PERFORMING ORGANIZATION REPORT NUMBER

9. SPONSORING/MONITORING AGENCY NAME(S) AND ADDRESS(ES)
Air Force Research Laboratory
Materials and Manufacturing Directorate
Wright-Patterson Air Force Base, OH 45433-7750
Air Force Materiel Command
United States Air Force

10. SPONSORING/MONITORING AGENCY ACRONYM(S)
AFRL/RXLMN

11. SPONSORING/MONITORING AGENCY REPORT NUMBER(S)
AFRL-RX-WP-TP-2010-4110

12. DISTRIBUTION/AVAILABILITY STATEMENT
Approved for public release; distribution unlimited.

13. SUPPLEMENTARY NOTES
Journal article submitted to the *International Journal of Plasticity*. PAO Case Number: 88ABW-2009-3901; Clearance Date: 09 Sep 2009. Paper contains color.

14. ABSTRACT
There is a need for accurate descriptions of the mechanical state of single crystal materials blades in gas turbine engines. These components are subject to such extreme temperatures and stresses that life prediction becomes highly inaccurate resulting in components that can only be shown to meet their requirements through experience. To help reduce this inadequacy in current design systems we have developed a thermo-viscoplastic constitutive model for single crystal materials. Our formulation additively decomposes the inelastic strain rate into components along the octahedral and cubic slip planes. Each of these is further additively decomposed into a time dependent creep component and a time independent plastic component. The strain rates are then incorporated into a large strain formulation. We formulate two robust and computationally efficient rate-independent crystal plasticity formulations. The transient variation of each of the plastic components includes a back stress for kinematic hardening and latent hardening parameters to include the increase of the stress with inelastic strain.

15. SUBJECT TERMS
single crystal materials blades, thermo-viscoplastic, inelastic strain rate

16. SECURITY CLASSIFICATION OF:			17. LIMITATION OF ABSTRACT:	18. NUMBER OF PAGES	19a. NAME OF RESPONSIBLE PERSON (Monitor)
a. REPORT	b. ABSTRACT	c. THIS PAGE			Reji John
Unclassified	Unclassified	Unclassified	SAR	34	19b. TELEPHONE NUMBER *(Include Area Code)* N/A

Standard Form 298 (Rev. 8-98)
Prescribed by ANSI Std. Z39-18

Introduction

In recent years a lot of attention has been paid to the analysis of the structures and parts operating under extreme thermal and mechanical loads. Special interest has arisen in the high temperature turbine parts which subject to long term viscoplastic deformations as well as time independent inelasticity caused by high level of mechanical stress. This combination of creep and plasticity leads to the damage nucleation and growth and a significant reduction of the part expected service life. Accurate prediction of material response for combined creep and plasticity deformations is a complex problem greatly compounded during cyclic loading. During the air foil service the strain controlled cyclic elastic-plastic deformations corresponding to airplane maneuvers are combined with so-called dwell times causing viscoplastic effects such as creep and/or stress relaxation. The development of unified creep – plasticity model capable of predicting cyclic non-isothermal loading conditions is of extreme importance.

Our constitutive models are based on state variables representing creep, plasticity and damage evolution. The basic physical mechanism of the inelastic deformation analyzed in this paper is dislocation glide or so-called crystallographic slip. We study the Ni-based superalloy PWA 1484 having $L1_2$ crystallographic structure. Deformation occurs along 12 octahedral slip systems {111}<110> and along 6 cube slip systems {001}<110>. Since the cube systems slip resistance is higher than the octahedral systems, the cube systems activity is limited. However, at high temperature and for initial crystallographic orientations close to <111> the γ' particles are sheared by cube systems. (C. Allan 1995, Stouffer and Dame 1996). Please see Table 1 for the slip system nomenclature in a single crystal superalloy.

Because of the wide temperature range the parts have been exposed during the service the inelastic deformation might be decomposed into creep and plasticity parts. At high temperatures the creep is a dominant mode of deformation and due to stress re-distribution the applied stress level remains at moderate levels and does not cause plastic deformation. The description of the creep model is given in Staroselsky and Cassenti (2008). However, when the part is being cooled down creep simply disappears and inelastic deformation takes place by crystallographic slip which does not vary with temperature as strongly as creep. Our creep experiments show that creep rates follow Arrhenius type relationship with the value of the activation energy varying in the range from $Q_{<001>} = 6.97E-19$ to $Q_{<111>} = 7.30E-19$ $J/atom$ with some stabilization (decrease of the activation energy) for the temperatures below 700 C. Plasticity plays the major role in residual stress generation during the cooling stage of TMF process.

In a rate dependent approach a constitutive law for the slip rate is assumed, usually in the power law form (for example, Asaro R.J. 1983, Asaro R.J. , Needleman, A. 1985, Kalidindi et al. 1992). This means that slip systems are active even before the resolved shear stress reaches critical values. The rate of inelastic deformation is proportional to the power of the effective resolved shear stress and the corresponding boundary value

problem has a unique solution. The higher the exponent in the power law the closer this approach gets to the classical plasticity theory. However, the price one has to pay for this is the increase in computational stiffness of the problem and an increase in the computational time. Nevertheless rate-dependent power law has demonstrated its efficiency and has been widely applied for both monotonic and cyclic problems of plasticity. However, when plastic analysis is combined with creep predictions, the rate dependent nature of the plastic part of the flow rule might cause some problems. A very good example is the inelastic analysis of single crystals of Ni-based superalloys which has a high creep rate at stresses of the order of two thirds of the yield. Let us consider a typical (Nissley, D. et al 1991, Staroselsky and Cassenti, 2008) rate depended model where the set of calibration parameters are as follows:

$\dot{\gamma}^{\alpha} = \dot{\gamma}_0 \left(\frac{\tau^{\alpha}}{s^{\alpha}} \right)^m$, where $\gamma_0 = 0.0001\,\mathrm{sec}^{-1}$ and m=30. It is important to note that there are only two independent parameters in such a formulation: $\frac{\gamma_0}{s^m}$ and the exponent m. Calibration is based on the computational predictions of plastic response to be in a good accord with experimental observations. Then, after 100 hours of creep at the stress level of 80% of yield the rate depended plastic term will predict the "creep" of approximately 5% , which is more than a quarter of total observed inelastic deformation to failure. The plastic term predictions interfere with creep prediction the closer the applied load is to yield. This problem might be eliminated by increasing the exponent to the level of 80 and higher, as shown in (Kalidindi and Anand, 1994) but this leads to its greater computational difficulties. Therefore there is a need for the further development of rate-independent crystal plasticity and combination with viscous terms. Also, it is important to note that rate sensitivity of Ni-based superalloys is small, which in turn leads to high values of the exponent.

We use two approaches to describe the rate independent behavior of single crystal materials. The first one is based on the concept of the potentially active systems and is reduced to the system of linear equations for the slip shear increments. The trial elastic increment is used to select the potentially active slip systems and to construct the linear equations. The idea of the method was originally formulated for the slip systems in FCC crystals under monotonic loading conditions by Anand and Kothari (1996) and generalized for combination of slip and twin systems by Staroselsky and Anand (1998). The second, more general approach uses the idea that the plastic strain rate is proportional to the total energy rate. Basically, by cancelling the derivatives, we come to the rate-independent formulation. Some of the earliest possible formulations were proposed by Kremple (1976), Valanis (1976), and Walker (1980). Later an isotropic version developed by Cassenti (1983) was shown to reduce in the limit to classical plasticity. The formulation required only two new temperature dependent material parameters. One was the yield stress and the other was a curvature parameter that can provide a gradual transition form a smooth uniaxial stress-strain curve to a stress-strain curve with a sudden change from the elastic slope to a perfectly plastic response. Both isotropic and kinematic hardening were included using the time dependent creep formulation. We generalize the formulation of Cassenti to single crystal materials and

add an appropriate power law to make the formulation agree exactly with a perfectly plastic formulation described in the first method. In this paper we focus on the development of generic rate-independent crystal plasticity models suitable for cyclic non-isothermal elastic-plastic-viscoplastic analysis.

The plan of the paper is as follows: We start section 2 with generalization of the rate-independent crystal plasticity model developed by Anand and Kothari (1996) to cyclic deformations. Then, we formulate the new rate-independent model which combines the advantages of both rate-dependent power method and with a rate-independent approach. We will compare the computational results obtained by all of these approaches for corner (symmetric) and a non-corner (single slip) initial crystal orientations. We will discuss slip system activities for different crystallographic orientations including octahedral and cube slip systems in the section 4. In the next section we will apply the developed rate-independent plasticity approach to the modeling of simple tension specimen and compare texture evolution, numerical stability, and necking effects with homogeneous numerical solutions and available experimental results. Section 6 provides results of model predictions of cyclic deformations of Ni-based superalloy and compares them against coupon testing results. We close the paper with some concluding remarks.

2. Governing Equations

The overall plastic response is taken as a sum of responses from small regions of a single crystal playing the role of representative volume elements (RVE). The deformation of a crystal is taken as the sum of contributions from overall elastic distortion and plastic deformation.

The governing variables in the constitutive model are as follows: the Cauchy stress tensor $\mathbf{T}$ and the deformation gradient $\mathbf{F}$. Each crystal slip system is specified by a unit normal to the slip plane $\mathbf{n}_0^\alpha$ and a unit vector along the slip direction $\mathbf{m}_0^\alpha$.

The total deformation gradient is multiplicatively decomposed on elastic and plastic parts as

$$\mathbf{F} = \mathbf{F}^e\mathbf{F}^p \quad \text{and} \quad \det\mathbf{F}^p = 1. \tag{1}$$

The elastic deformation gradient $\mathbf{F}^e$, $(\det\mathbf{F}^e > 0)$ describes elastic distortion and gives rise to the stress $\mathbf{T}$. The constitutive equation for the second Piola-Kirchoff stress tensor is taken as a linear relation:

$$\mathbf{T^*} = L\left[\mathbf{E}^e\right]^{\dagger};\ \text{where}\ \mathbf{E^e}(\tau) = \tfrac{1}{2}\left(\mathbf{C^e}(\tau) - \mathbf{I}\right);\ \text{and}\ \mathbf{C^e(\tau)} = \mathbf{F^{eT}F^e} \tag{2}$$

at the current moment of time denoted, τ.

The Cauchy stress tensor is the work conjugate stress corresponding to the Cauchy – Green elastic strain measure and is calculated as follows:

---

† Generally speaking the elastic relation looks as follows: $\mathbf{T^*} = L\left[\mathbf{E}^e - \mathbf{A}\left(\Theta - \Theta_0\right)\right]$, where $\mathbf{A}$ is thermal expansion tensor, Θ is current temperature and Θ_0 is the reference temperature. All results we report in this paper are valid and derived general formulae and algorithms do not change when we add this thermal strain term. For the sake of simplicity we will use formula (2) in this paper.

$$\mathbf{T} = \frac{1}{\det(\mathbf{F^e})}\mathbf{F^e T^* F^{eT}} \tag{3}$$

The evolution equation for the viscoplastic deformation gradient is given by the flow rule:

$$\dot{\mathbf{F}}^p = \mathbf{L}^p\mathbf{F}^p \text{ where } \mathbf{L}^p = \sum_{slip\ systems} \dot{\gamma}^\alpha \mathbf{S}^\alpha \quad \text{and} \quad \mathbf{S}^\alpha = \mathbf{m}^\alpha \otimes \mathbf{n}^\alpha \tag{4}$$

The shear rate along each slip system $\dot{\gamma}^\alpha$ is given in terms of the resolved shear stress (RSS) $\tau = \mathbf{T}^* \bullet \mathbf{S}^\alpha$, slip systems resistances and equilibrium back stress. Evolution of crystallographic texture is explicitly defined by the elastic part of deformation gradient.

$$\begin{aligned} \mathbf{m}_\mathbf{t}^\alpha &= \mathbf{F^e m}_\mathbf{0}^\alpha \\ \mathbf{n}_\mathbf{t}^\alpha &= \mathbf{F}^{\mathbf{e}-\mathbf{T}}\mathbf{n}_\mathbf{0}^\alpha \end{aligned} \tag{5}$$

In order to complete the calculations one has to be able to calculate slip systems shear rate or slip systems shear increment in an incremental formulation. In rate-dependent model this problem has been resolved by defining a power law viscoplastic relation with a back stress: for the inelastic strain rate along α–th slip system:

$$\{\dot{\gamma}\}^\alpha = \dot{\gamma}_0 \left| \frac{\frac{\tau^\alpha}{(1-d_v)} - \omega^\alpha}{s_*^\alpha} \right|^n \operatorname{sgn}\left(\tau^\alpha - \omega^\alpha\right), \tag{6}$$

where $\dot{\gamma}_0$ is a temperature dependent time constant, and s^α is the deformation resistance of α-th slip system; τ^α is resolved shear stress, ω^α is the slip system back stress, *n* is the creep exponent which is very high (~80) to simulate plastic response, d_v is the void related damage parameter, and $(\dot{\ })$ is the rate of change with respect to time.

Next, latent hardening evolution has been described by modifying Asaro's (1983) hardening rule $\dot{s}^\alpha = h_0\left(1 - \frac{s^\alpha}{s^*}\right)^p \sum_\beta h^{\alpha\beta}\left|\dot{\gamma}^\beta\right|$, with hardening matrix $h^{\alpha\beta} = \left\{q + (1-q)\delta^{\alpha\beta}\right\}$ for temperature dependent h_0 and $s*$. We model cyclic effects by defining for each slip system a specific internal equilibrium, or back stress ω. The back stress has a limiting saturation value $\omega_\infty = \frac{c_1}{c_2}$, corresponding to the stabilization of the equilibrium portion of the stress (i.e., the portion of the stress that has not yet contributed to the inelastic strain) and evolves according to the following relationship (Nissley, D., et al, 1991, Voyiadjis, G.Z., Huang, W., (1996), Stouffer, D.C., and Dame, L.T (1996)):

$$\dot{\omega}^\alpha = c_1\dot{\gamma}^\alpha - c_2\left|\dot{\gamma}^\alpha\right|\omega^\alpha \tag{7}$$

Equation (7) requires two additional coefficients c_1 and c_2 that are explicit functions of temperature. The effect of voids on the slip rate can be calculated through a correction of

the effective stress: $\left(\frac{\frac{\tau^{\alpha}}{(1-d_v)} - \omega^{\alpha}}{s_*^{\alpha}} \right)$ (an effective increase in the resolved shear stress). This is equivalent to a Kachanov-type damage parameter (Kachanov 1986, Lemaitre 1996) . For the sake of simplicity we will not consider the effects of voids in this paper.

3. Generalization of incremental linear system formulation to cyclic plasticity.

One of the major problems of crystal plasticity is to determine the unique set of the active slip systems and their corresponding shear rates at each time increment. At each strain increment, only five strain components can be uniquely prescribed. Because the number of slip systems for FCC systems are 12 and for $L1_2$ structures are 18, the problem of selecting active ones is crucial. In a power law model all slip systems are active just the value of slip rate might be infinitesimal if the resolved shear stress is small. If the value of exponent is small (from 3 to 5), which is the case for creep phenomena, then the slip systems with significant but not the largest values of the resolved shear stress (RSS) are still active and the total shear along these "second order" slip systems could be significant. In the rate independent (RI) model, the system might be active only if the effective RSS is equal to slip resistance (i.e., the yield stress). Then

$$\dot{\gamma}^{\alpha} \geq 0 \text{ if and only if } \left|\tau^{\alpha} - \omega^{\alpha}\right| = s^{\alpha}(\tau). \tag{8}$$

In this section we will reduce the problem to the systems of the linear equations with respect to shear increments. This system should be solved at each incremental step using any numerical method minimizing errors for example, the method of singular value decomposition (SVD), which will define the unique solution for the plastic strain in L_2 norm sense (Anand and Kothari 1996) or penalty functions (Staroselsky and Anand 1998).

We use an incremental formulation where we define all parameters at the end of the time increment $\tau = t + \Delta t$ based on state in the beginning of the increment at time t. Expression (4) has the incremental form as follows:

$$\mathbf{F}^{p}(\tau) = \mathbf{L}^{p}(\tau)\mathbf{F}^{p}(t) = (\mathbf{1} + \sum_{\alpha} \Delta\gamma^{\alpha}\mathbf{S}_0^{\alpha})\mathbf{F}^{\mathbf{p}}(t) \tag{9}$$

We need to express elastic Cauchy-Green tensor through total and plastic deformation gradients using equations (1) and (2) as:

$$\mathbf{C}^{\mathbf{e}}(\boldsymbol{\tau}) = \mathbf{F}^{p-\mathbf{T}}\mathbf{F}^{T}\mathbf{F}\mathbf{F}^{p-1} \tag{10}$$

Numerical integration is taken using a forward Euler integration scheme. In order to perform it within this RI model, we define a trial step where we assume that the whole increment is elastic. The stress overshoot is compensated for by crystallographic slip. The constitutive relations for the trial step are taken as follows:

$$\begin{aligned}
&\mathbf{T}^{*tr} = L\left[\mathbf{E}^{etr}(\tau)\right], \\
&\mathbf{E}^{e\ tr}(\tau) = \tfrac{1}{2}\left(\mathbf{C}^{etr}(\tau) - \mathbf{I}\right), \text{ and} \\
&\mathbf{C}^{etr}(\boldsymbol{\tau}) = \mathbf{F}^{etr\,\mathrm{T}}\mathbf{F}^{etr}.
\end{aligned} \tag{11}$$

Where

$$\mathbf{F}^{etr}(\tau) = \mathbf{F}(\tau)\mathbf{F}^{p}(t)^{-1} \tag{12}$$

and the trial resolved shear stress along each slip system is

$$\tau^{\alpha tr} = \mathbf{T}^{*tr} \bullet \mathbf{S}_0^{\alpha}. \tag{13}$$

Substituting (12) into (11) and using expressions (9) and (10) one can obtain the relationship between true and trial stress tensors (Kalidindi, et al 1992), which already accounts for the amount of incremental shear, as:

$$\mathbf{T}^{*} = \mathbf{T}^{*tr} - \sum_{\alpha} L\left[sym\left(C^{etr} S_0^{\alpha}\right)\right]\Delta\gamma^{\alpha} \tag{14}$$

and similarly for the resolved shear stresses

$$\begin{aligned}
\tau^{\alpha} &= \tau^{\alpha tr} - \sum_{\beta} L\left(sym\left(\mathbf{C}^{etr}\mathbf{S}_0^{\beta}\right)\right)\mathbf{S}_0^{\alpha}\Delta\gamma^{\beta} = \\
&= \tau^{\alpha tr} - \sum_{\beta} L\left(sym\left(\mathbf{C}^{etr}\mathbf{S}_0^{\beta}\right)\right)\mathbf{S}_0^{\alpha}\left|\Delta\gamma\right|^{\beta} sign\left(\tau^{\beta tr} - \omega^{\beta}\right)
\end{aligned} \tag{15}$$

At the next step, following the idea of Anand & Kothari (1996) we assume that during small strain increment, changes in the slip directions defined as $\mathrm{sign}\left(\Delta\gamma^{\alpha}(\tau)\right) = \mathrm{sign}\left(\tau^{\alpha}(\tau) - \omega^{\alpha}(\tau)\right)$ would:

(i) be the same for the true and trial increments $\mathrm{sign}\left(\tau^{\alpha} - \omega^{\alpha}\right) = \mathrm{sign}\left(\tau^{\alpha tr} - \omega^{\alpha tr}\right)$, and

(ii) the effect of change in back stress values during one increment does not affect the slip direction: $\mathrm{sign}\left(\tau^{\alpha}(\tau) - \omega^{\alpha}(\tau)\right) = \mathrm{sign}\left(\tau^{\alpha}(t) - \omega^{\alpha}(t)\right)$.

We need these assumptions in order to compute absolute values of the effective resolved shear stress used for the yield criteria

$$\left|\tau^{\alpha} - \omega^{\alpha}\right| = s^{\alpha}(\tau) \tag{8}$$

The systems for which trial values of effective shear stress are less than slip resistance in the beginning of increment *s(t)* are called inactive and are not analyzed during the increment. For the other or so-called "potentially active" slip systems, the absolute value of the effective shear stress can be calculated through the resolved shear stress trial value.

$$\left|\tau^{\alpha} - \omega^{\alpha}\right| = \left|\tau^{\alpha tr} - \omega^{\alpha}(\tau)\right| - \sum_{\beta} L\left(sym\left(\mathbf{C}^{etr}\mathbf{S}_0^{\beta}\right)\right)\mathbf{S}_0^{\alpha}\left|\Delta\gamma\right|^{\beta} sign\left(\tau^{\beta} - \omega^{\beta}\right) sign\left(\tau^{\alpha} - \omega^{\alpha}\right) \tag{16}$$

By the use of the incremental formulation for the back stress (7):

$$\omega^{\alpha}(\tau) = \omega^{\alpha}(t) + \left(C_1 sign(\Delta\gamma^{\alpha}) - C_2\omega^{\alpha}(t)\right)\left|\Delta\gamma^{\alpha}\right|$$

We immediately obtain that

$$\left|\tau^{\alpha\,tr} - \omega^{\alpha}(\tau)\right| = \left|\tau^{\alpha\,tr} - \omega^{\alpha}(t)\right| - \left(C_1 - C_2\omega^{\alpha}(t)\right) sign\left(\tau^{\alpha\,tr} - \omega^{\alpha}(t)\right)\left|\Delta\gamma^{\alpha}\right| \tag{17}$$

And finally, using the latent hardening evolution equation $s^{\alpha}(\tau) = s^{\alpha}(t) + \sum_{\beta} h^{\alpha\beta}\left|\Delta\gamma^{\beta}\right|$ we reduce the problem of finding absolute values of slip increments determination to a solution of the linear system,

$$\mathbf{B}\left|\boldsymbol{\Delta\gamma}\right| = \mathbf{b} \tag{18}$$

where

$$B^{\alpha\beta} = h^{\alpha\beta} + \left(C_1 - C_2\omega^{\alpha}(t)\right) sign\left(\tau^{\alpha\,tr} - \omega^{\alpha}(t)\right) + \mathbf{S_0^{\alpha}} L\left(sym\left(\mathbf{C}^{e\,tr}\mathbf{S_0^{\beta}}\right)\right) sign\left(\tau^{\beta\,tr} - \omega^{\beta}\right) sign\left(\tau^{\alpha\,tr} - \omega^{\alpha}\right)$$
$$b^{\alpha} = \left|\tau^{\alpha\,tr} - \omega^{\alpha}(t)\right| - s^{\alpha}(t). \tag{19}$$

This system has a number of variables equal to the number of "potentially active" slip systems, however not all of the linear equations are always linearly independent. The system might be solved using any appropriate approximation scheme from linear algebra. One of the "proven" and effective algorithms is SVD which gives the least square solution. We do not discuss the advantages and disadvantages of different linear algebra algorithms and use that numerical approach throughout this paper.

4. Time-independent formulation

In the previous section we have described the rate independent plasticity calculations by using approximate solution of a linear system. This is the limiting case when the yield surface is well-defined. However, there is still a need to combine the advantages of a continuous rate independent plastic behavior description. This is especially true for cyclic non-isothermal conditions present in thermal mechanical fatigue (TMF). Such a formulation would automatically include the characteristic variation in yield surfaces between materials. In this section we formulate our new rate-independent flow rule and compare the deformation and slip activities model predictions against classical power law as well as the linear system rate-independent method described above.

We include a time independent inelastic strain by an additive decomposition of the deformation velocity gradient into three parts: elastic, the time dependent creep strain rate, and a time independent plastic one. We can insure that the plastic strain rate is time independent by making it proportional to another rate. Let us consider the example, a plastic strain rate that is proportional to the plastic work rate, $\dot{W}^{p}$, then

$$\dot{\varepsilon}_{ij}^{p} = \frac{d\varepsilon_{ij}^{p}}{dt} = f\left(\dot{W}^{p}\right)\dot{W}^{p} = f\left(\dot{W}^{p}\right)\frac{dW^{p}}{dt} \tag{20}$$

and the differentials will cancel each other in an integration to yield

$$\frac{d\varepsilon_{ij}^{p}}{dW^{p}} = f\left(\dot{W}^{p}\right). \tag{21}$$

Equation (21) makes ε_{ij}^{p} a function of W^{p} independent of any rates, and subsequently the model is rate-independent. Now, let us apply this concept to formulate a crystal plasticity rate-independent flow rule.

For each of the slip systems the inelastic strain rate, $\dot{\gamma}^{\alpha}$, is a function of the effective stress for that slip system, $\tau_{\alpha} - \omega_{\alpha}$, and we could choose,

$$\dot{\gamma}^{\alpha} = \frac{\tau^{\alpha} - \omega^{\alpha}}{\sigma_{\infty}^{2}} < \dot{W}^{p} > \tag{22}$$

where $\langle x \rangle$ is the unit ramp function of x and σ_{∞} is a temperature dependent material parameter. Expression (22) is deficient since a slip system will be active with noticeable shear rate even for relatively moderate values of the effective resolved shear stress, which is much less than one for actually active slip systems. This can be corrected by modifying equation (22) through the use of a power law in the effective resolved shear stress as follows:

$$\dot{\gamma}^{\alpha} = \frac{\tau^{\alpha} - \omega^{\alpha}}{\sigma_{\infty}^{2}} \left| \frac{\tau^{\alpha} - \omega^{\alpha}}{s} \right|^{m} \left\langle \dot{W}^{p} \right\rangle. \tag{23}$$

Here we used the fact that power function with the argument varying from zero to unity behaves almost like a switch function for high powers where the closer to ideal switch (Heaviside function) the higher the exponent is. In our case we use values of the exponent $m \le 30$ which guarantees good selection of slip activities and free of the computational problems specific for power models with very high values of the exponent values.

Equation (23) has assumed that only the plastic work contributes to the plastic strain, but the total work rate may also be an important variable. Since $\dot{W}^{p} = \dot{W} - \dot{W}^{e}$, we can use a weighted sum of the total and elastic work rates by replacing the plastic work rate with a weighted sum in equation (23) in the following way:

$$\dot{\gamma}^{\alpha} = \frac{\tau^{\alpha} - \omega^{\alpha}}{\sigma_{\infty}^{2}} \left| \frac{\tau^{\alpha} - \omega^{\alpha}}{s} \right|^{m} \left\langle \dot{W} - k\left(\dot{W} - \dot{W}^{p}\right) \right\rangle \tag{24}$$

where k is a temperature dependent material parameter. The total work rate is given by

$$\dot{W} = \sum_{i,j} \sigma_{ij} \dot{\varepsilon}_{ij} = \sigma_{ij} \dot{\varepsilon}_{ij}, \tag{25}$$

and the plastic work rate is

$$\dot{W}^{p} = \sum_{\alpha} \left(\tau_{\alpha} - \omega_{\alpha}\right) \dot{\gamma}^{\alpha}. \tag{26}$$

Substituting equation (26) into equation (24) for the plastic work rate and solving equation for $\dot{W}^{p}$ yields

$$\dot{W}^{p} = \frac{(1-k)\langle \dot{W} \rangle \sum_{\alpha} \left(\frac{\tau^{\alpha} - \omega^{\alpha}}{\sigma_{\infty}^{2}} \right)^{2} \left| \frac{\tau^{\alpha} - \omega^{\alpha}}{s} \right|^{m}}{1 - k \sum_{\alpha} \left(\frac{\tau^{\alpha} - \omega^{\alpha}}{\sigma_{\infty}^{2}} \right)^{2} \left| \frac{\tau^{\alpha} - \omega^{\alpha}}{s} \right|^{m}}. \tag{27}$$

Substituting equation (28) into equation (24) yields

$$\dot{\gamma}^{\alpha} = \frac{(1-k)\langle \dot{W} \rangle \frac{\tau^{\alpha} - \omega^{\alpha}}{\sigma_{\infty}^{2}} \left| \frac{\tau^{\alpha} - \omega^{\alpha}}{s} \right|^{m}}{1 - k \sum_{\alpha} \left(\frac{\tau^{\alpha} - \omega^{\alpha}}{\sigma_{\infty}^{2}} \right)^{2} \left| \frac{\tau^{\alpha} - \omega^{\alpha}}{s} \right|^{m}}. \tag{28}$$

Identifying σ_{∞} with s in the equation (28) and assuming that state variable s might be different for different slip systems we get the final form for the rate independent plastic strain rate, we can write

$$\dot{\gamma}^{\alpha} = \frac{(1-k)\left\langle \frac{\dot{W}}{s^{\alpha}} \right\rangle \left| \frac{\tau^{\alpha} - \omega^{\alpha}}{s^{\alpha}} \right|^{m+1}}{1 - k \sum_{\alpha} \left| \frac{\tau^{\alpha} - \omega^{\alpha}}{s^{\alpha}} \right|^{m+2}}. \tag{29}$$

Thus, we formulated the rate-independent flow rule and introduced one more parameter $0 \le k < 1$. If the value of this parameter is close to zero, yield values change gradually as it usually observed during the deformation hardening. In the limiting case of $k \to 1$ (in Eq. 29) there will be a sudden change in the plastic strain rate when $\tau^{\alpha} - \omega^{\alpha} = s^{\alpha}$, and, hence, s^{α} can be interpreted as a yield stress. Interestingly enough that graduate hardening behavior is correlated to the partial amount of dissipated energy proportional to the yield strain increment. Typical stress-strain curves with different values of parameter k are shown in Fig. 1.

5. Model Implementation and Evaluation of the Parameters

In this section we compare the predictions obtained by our new rate independent plasticity model against predictions obtained by a power law, and the solution of the linear system described in section 2, with available experimental data. We discuss single crystal Ni-based superalloy constitutive behavior at relatively high temperatures where the loading applied along one of the corner orientation <001> or <111> and along an internal orientation of $< \bar{2}36 >$ and $< \bar{1}23 >$.

Anisotropic elastic properties are defined by three different moduli that are changed with temperature and shown in Fig. 2. The fourth order elasticity tensor has the form specific for orthotropic materials with cubic symmetry:

$$C_{iiii} = C11; \quad (i = 1, 3)$$
$$C_{iijj} = C12; \quad (i, j = 1, 3)$$
$$C_{ijij} = C44; \quad (i, j = 1, 3)$$

We consider single crystal Asaro hardening behavior $\dot{s}^{\alpha} = h_0 \left(1 - \frac{s^{\alpha}}{s^{*}}\right)^{p} \sum_{\beta} h^{\alpha\beta} \left|\dot{\gamma}^{\beta}\right|$ where the parameters h_0 and initial value of slip resistance s_0 for both octahedral and cube systems are also functions of temperature. Results of slip resistance calibration against experimental data are shown in Fig 3. Due to low strain hardening of PWA1484 for some example calculations we use a non-hardening model.

Using the developed constitutive models we perform simulations of displacement controlled simple tension tests. We use ANSYS ET 185 8-node brick elements for both single element and 3744-element cylinder simulations. Single element simulations satisfy homogeneous uniaxial stress and strain distribution. Analysis shows that two types of boundary conditions provide the required uniaxial stress-strain distribution. We will call the single element with the following boundary conditions: upper and lower surfaces remain parallel and orthogonal to the displacement direction, the element type A. The element with two vertical sides parallel to the loading direction will be called the element type B. Both elements and sketches illustrating the deformation of each type are shown in Fig. 4 (from Dieter, 1988).

There is no numerical difference between predictions of single elements for A or B types subject to simple tension of high symmetry corner orientation <001> and <111> due to highly homogeneous deformation. Moreover, the single element prediction is exactly the same as the numerical predictions obtained from cylinder calculations. Crystal orientation does not change during the numerical tests in both corner orientations. There are eight equally active octahedral systems for <001> crystallographic orientation tests. The normalized stress-strain curves obtained by methods described above and also experimentally measured for 980 C are shown in Fig 5a. There are six equally active octahedral slip systems $(111)[\bar{1}01]$, $(111)[01\bar{1}]$, $(\bar{1}1\bar{1})[011]$, $(\bar{1}1\bar{1})[10\bar{1}]$, $(\bar{1}\,\bar{1}1)[0\bar{1}\,\bar{1}]$ and $(\bar{1}\,\bar{1}1)[\bar{1}10]$ as well as 3 identically active cube slip systems $(100)[011]$, $(010)[10\bar{1}]$, and $(001)[1\bar{1}0]$ observed during simulations of simple tension along a <111> crystallographic orientation. State variables have been calibrated in such a way that cube slip system shear is two orders of magnitude larger than octahedral slip shear. The normalized stress-strain curves for this crystallographic orientation at 980 C are shown in Fig 5b.

When loaded along a central direction inside the primary stereographic triangle the single crystal deforms initially along a single slip system with the highest value of resolved shear stress (i.e., with the highest value of Schmidt factor). Usually such a deformation is very unstable. We conducted simple tension simulations (type A) of a single crystal along $<\bar{2}36>$ crystallographic direction. The stress-strain curves for

980 C are shown in Fig 6. The slip system activity is shown in Fig. 7. Deformation starts with a single octahedral slip system $(111)[\bar{1}01]$, then when the strain reaches about 8% the second conjugate slip system $(11\bar{1})[011]$ becomes active. It is important to note that the cube slip system $(001)[1\bar{1}0]$ is also active from the beginning, as can be seen from the plots in Fig. 7, but the total amount of cube slip system shear is much less than due to octahedral slip systems. The slip resistance of the conjugate slip system is bigger than the slip resistance of the active one due to latent hardening. The effective resolved shear stress reaches the critical value at deformation levels slightly larger than for the non-hardening case[‡] and subsequently the re-orientation slightly overshoot the stereographic triangle boundary $[001]-[\bar{1}11]$. After activation of the conjugate slip system $(11\bar{1})[011]$ the lattice rotates toward the $[\bar{1}11]$ pole along the triangle boundary. The prediction of our rate-independent model is indistinguishably close to the predictions obtained by the solution of the linear system and by the power law (rate-dependent model) with the exponent higher than 80. It is important to note that the rate-dependent power law with small values of exponent specific for creep (3 to 5) predicts that more slip systems are active leading to more homogeneous deformation and slower crystal re-orientation. For example, for creep along $<\bar{2}36>$ crystallographic orientation slip systems $(111)[01\bar{1}]$ and $(1\bar{1}\,\bar{1})[\bar{1}0\bar{1}]$ are also active, however total slip along these systems is significantly smaller than along the primary and the conjugate ones.

Deformation along $<\bar{2}36>$ is very sensitive to the boundary conditions. The stress-strain relationship obtained under different types of boundary conditions, such as Type A as was reported above, type B loading as well as numerical results from the cylinder specimen model is shown in Fig. 8. Deformation takes place along the single $(111)[\bar{1}01]$ slip system till collapse occurs by excessive deformation. Crystal reorientation is rotated slightly toward the $[001]$ pole from the boundary conditions as shown in Fig. 9 together with prediction obtained for type A loading. We evaluated the one element prediction by comparing the numerical results against our 3744-element cylinder specimen model. The top and bottom of the numerical specimen are rigidly prevented from rotation and absolutely symmetric. In order to eliminate end-effects the last 2 layers of finite elements from each end are made elastic. We use 35 elastic-plastic central layers of finite elements and 96 elements in each cross-section as shown in Fig 10. Deformation is very sensitive to a minor variation of boundary conditions and starts necking at deformation levels of about 7-10% as shown in Fig 11. An increase in the number of elements at least within the same order of magnitudes does not change the character of deformation which appears to be very inhomogeneous. The central elements deform almost according to loading scheme A, while surface and near surface elements clearly deforms as type B elements. Due to inhomogeneities in the deformation the crystal lattice reorientation of the central element is different than type A results but reasonably close to it as can be seen from Fig. 9. Due to the lack of the symmetry during the deformation the model predicts noticeable ovalization of the cross-section as shown

[‡] We performed modeling for the "theoretical" non-hardening case and the conjugate slip system became active exactly on the boundary of stereographic triangle.

in Fig. 12. Such an ovalization is specific for any non-corner crystallographic orientation and might be used for specimen life prediction as has been shown by D. Shah et al (2004).

Most of the RI models used deal with monotonic loading response, but here we apply our approaches to cyclic loading schemes and verify our simulation predictions against test results obtained on PWA 1484 Ni-based superalloy at isothermal conditions. There are several well known observations that should be modeled while analyzing the cyclic tests:

(i) Bauschinger effect –initial reduction of the reverse proportional limit and
(ii) Cyclic softening- reduction of initially high hardening rate due to cyclic transient effects (Watanabe et al 2002, Xu and Jiang 2004).

The Bauschinger effect is controlled by the evolution equation for the back stress $\omega(t)$ (see the eq. 7). During the reverse cycle the back stress is still not yet steady and the absolute value of the effective stress $|\tau - \omega|$ reaches the critical value earlier than during the initial "forward" loading step. Experimental results (C.C Lin 1995) indicate that the cyclic softening effects are active only during transient regime which is approximately equal to the time needed for the back stress to change sign. We simulated this effect by adding a latent cyclic softening term proportional to the terms depended on $sign(\omega \cdot \dot{\gamma}^{\alpha})$ as follows:

$$\varsigma^{\alpha} = \tfrac{1}{2}\left(2 - \eta + \eta sign(\omega^{\alpha} \cdot \dot{\gamma}^{\alpha})\right) \tag{30}$$

where the parameter η has to be adjusted to reflect the intensity of cyclic softening. In our calculations, we used $\eta = 1$, which means that there is a non-hardening plateau during transient unloading. The latent hardening law has been modified as follows:

$$\dot{s}^{\alpha} = \varsigma^{\alpha}\ h_0\left(1 - \frac{s^{\alpha}}{s^{*}}\right)^{p} \sum_{\beta} h^{\alpha\beta}\left|\dot{\gamma}^{\beta}\right| \tag{31}$$

If the back stress and the effective RSS have the same signs the dislocation microstructure deforms in a similar to monotonic loading and the parameter $\varsigma \equiv 1$. Otherwise, if the signs of the back stress and slip shear rate are opposite the dislocation cells structure is dissolving and the hardening rate slows down. It is important to note that during any monotonic loading parameter $\varsigma \equiv 1$ and Eq. 31 becomes the classical Asaro hardening rule again.

Results of the model implementation against test data are shown in Figs 13-15. Figure 13 (a, b, c) shows a comparison of model prediction against experimental data for <001> single crystal PWA1484 cyclically loaded up to 1% of strain amplitude at a temperature of 870 C. Due to strain hardening the overall loops shift up in the stress-strain plane and the hysteretic loop is getting narrower. We present the modeling results together with measured test data for the first cycle (Fig 13 a) and cycle #10 (Fig 13 b), as well as cycle # 30 (Fig. 13 c) where the cyclic loop is stabilized. One can see that simulation results are extremely close to the test observations. Fig.14. shows stress-strain relations for <111> oriented single crystal cyclically deformed using strain control to the mechanical strain

range of 0.8% (actual magnitude is 0.41%) at temperature of 870 C. Due to the high Young's modulus the yield is more pronounced along the <111> orientation and the loop is wider open than at the similar loading conditions along the <001> crystallographic direction. Comparison of predicted vs. measured data demonstrates high quality of the model. Modeling results obtained for $< \bar{1}23 >$ single slip orientation compared against test data are shown in Fig. 15 for the isothermal conditions of 870 C and strain range of 0.8%.with R=-1. The deformation starts with $(111)[01\bar{1}]$ single slip system. The loop is extremely wide due to relatively low yield value for the single crystal along single slip crystallographic direction. Error of the numerical prediction is less than 10% which is good for a single slip crystallographic orientation. Model predictions can be improved by refining tension-compression asymmetry properties in the model. We did not pay attention to this issue in this work. The numerical results demonstrate that our developed elastic-plastic model is capable of obtaining extremely good predictions for both the monotonic and the cyclic plastic response of a $L1_2$ single crystal.

6. Concluding Remarks

The constitutive model developed has been implemented in the commercial finite element software ANSYS as a material user routine to predict yield anisotropy and yield –thermal dependence. The equations governing the mechanical response have been calibrated using existing experimental data. The model predicts the crystallographic lattice rotation during deformation, which is important during material processing and cyclic ratcheting, especially around geometrical features such as cooling holes in single crystal turbine blades. Our rate-independent cyclic crystal plasticity formulations are designed for cyclic and non-isothermal loading conditions. They can uniquely determine the amount of shear along active slip systems at each increment. The approaches developed are numerically robust and efficient, allowing numerical analysis of tens and even hundreds cycles providing a working tool for low cycle fatigue (LCF) and thermal mechanical fatigue (TMF) prediction analysis.

We have developed a rate independent model that can be readily applied to TMF over an extremely wide range of conditions which naturally reduces to our SVD approach as a limiting condition.
Based on our modeling results and their comparison with experiments it is possible to conclude the following:

(1) The major deformation mechanisms of high temperature creep of Ni-based single crystal superalloy are octahedral {111}(110) and cube {001}(110) crystallographic slip.
(2) Single slip crystallographic orientations deform mostly non-homogeneously, which leads to necking and subsequently shorter life.
(3) Ovalization of the plastically deformed single crystal specimen might be correlated with time to failure
(4) Strain hardening and cyclic softening can be accurately predicted.

The combined theoretical-numerical-experimental study of single crystal PWA 1484 Ni-based superalloy reported here represents the steps at understanding the difficult and important topic of visco-plastic deformation in $L1_2$ systems; it holds substantial promise through future work and through further refinement. In particular, the model will be used to more accurately account for the thermal-cyclic effects and for creep-plasticity interactions.

Acknowledgements

The authors are grateful for support and funding from the United States Air Force Research Laboratory through contract # FA8650-07-C-5252 and to Dr. Andrew Rosenberger for his support and attention to this work. Authors also would like to thank Prof. Alan Needleman for fruitful discussions.

References

Allan, C. (1995), Plasticity of Nickel Base Single Crystal Superalloys. Ph.D. Thesis, MIT

Stouffer, D.C., Dame, L.T., Inelastic Deformation of Metals, John Wiley & Sons, Inc. 1996

Anand, L., Kothari, M., (1996) A computational procedure for rate – independent crystal plasticity. J. Mech. Phys. Solids **44**, 525-558.

Asaro R.J. 1983, Crystal Plasticity, ASME J. Appl. Mech. **50**, 921-934

Asaro R.J., Needleman, A. 1985, Texture Development and Strain Hardening in Rate Dependent Polycrystals, Acta Metall. **33**, 923-953.

Cassenti, B.N.,(1983), Research and Development Program for the Development of Advanced Time-Temperature Dependent Constitutive Relationships - Vol. 1 - Theoretical Discussion, NASA CR-168191.

Dieter G.E. (1988) Mechanical Metallurgy, McGraw-Hill Co, London

L. M. Kachanov, Introduction to the Theory of Damage, Martinus Nijhoff, Hague, 1986

Kalidindi, S.R., Bronkhorst, C.A., and Anand L., (1992) Crystallographic Texture Evolution during bulk deformation processing of f.c.c. metals. J. Mech. Phys. Solids **40**, 537-569.

Kalidindi, S.R., and Anand L., (1994), Macroscopic shape change and evolution of Crystallographic in pre-textured f.c.c. metals. J. Mech. Phys. Solids **42**, 459-490

Krempl, E., C. H. Wells and Z. Zudans (1976): Workshop on Inelastic Constitutive Equations for Metals: Experimentation-Computation-Representation. Rensselaer Polytechnic Institute, Troy, New York.

Lemaitre, J. A course on damage mechanics. Springer, Berlin, 228 p., 1996

Lin, C.C. (1995), Cyclic deformation of FCC crystals, MS Thesis, MIT

Nissley, D., Meyer, T., and Walker, K. 1991, Life Predictions and Constitutive Models for Engine Hot Section Anisotropic Materials, Pratt & Whitney, Report NAS3-23939

Shah, D.M., S.Vega, S. Woodard, and A.D. Cetel, (2004), Primary creep in nickel-base superalloys in Superalloys 2004. Edited by K.A. Green, T.M. Pollock, H. Harada, T.E. Howson, R.C. Reed, J.J. Schirra, and S, Walston, TMS, pp. 197-206

Staroselsky, A. and Anand, L. (1998), Inelastic deformation of polycrystalline face centered cubic materials by slip and twinning. J. Mech. Phys. Solids. 46 (4), pp.671-696
Staroselsky, A. Cassenti B., (2008) Mechanisms for Tertiary Creep of Single Crystal Superalloy, Mech. Time-Depend. Mater. **12**, 275-289.
Valanis, K. C (1976), Constitutive Equations in Viscoplasticity: Phenomenological and Physical Aspects. AMD, Vol. 21, ASME..
Walker, K. P. (1980), Representation of Hastelloy-X Behavior at Elevated Temperature with a Functional Theory of Viscoplasticity. Presented at ASME/PVP Century 2 Emerging Technology Conference, San Francisco, California, August 1980.

Voyiadjis, G.Z., Huang, W., (1996) A modeling of single crystal plasticity with back-stress evolution. Eur. J. Mech. A 319-321, 63-73

Xu, B. and Jiang Y., (2004) A cyclic plasticity model for single crystal, Int. J. of Plasticity **20**, 2161-2178
Watanabe, C., Kanmuri, K.,Kato, M., Onaka, S., Fuji T., (2002) Re-arrangement of fatigue dislocation structure in copper single crystals associated with reduction in the plastic strain amplitude. Phil. Mag. **A 82**, 1317-1330

Table 1.

Slip systems operative in PWA1484 at high temperature

Octahedral

α	$(\mathbf{n}^{\alpha})[\mathbf{m}^{\alpha}]$
1	$(111)[01\bar{1}]$
2	$(111)[\bar{1}01]$
3	$(111)[01\bar{1}]$
4	$(1\bar{1}\,\bar{1})[0\bar{1}1]$
5	$(1\bar{1}\,\bar{1})[\bar{1}0\bar{1}]$
6	$(1\bar{1}\,\bar{1})[110]$
7	$(\bar{1}1\bar{1})[011]$
8	$(\bar{1}1\bar{1})[10\bar{1}]$
9	$(\bar{1}1\bar{1})[\bar{1}\,\bar{1}0]$
10	$(\bar{1}\,\bar{1}1)[0\bar{1}\,\bar{1}]$
11	$(\bar{1}\,\bar{1}1)[101]$
12	$(\bar{1}\,\bar{1}1)[\bar{1}10]$

Cube

α	$(\mathbf{n}^{\alpha})[\mathbf{m}^{\alpha}]$
13	$(100)[011]$
14	$(100)[01\bar{1}]$
15	$(010)[101]$
16	$(010)[10\bar{1}]$
17	$(001)[110]$
18	$(001)[1\bar{1}0]$

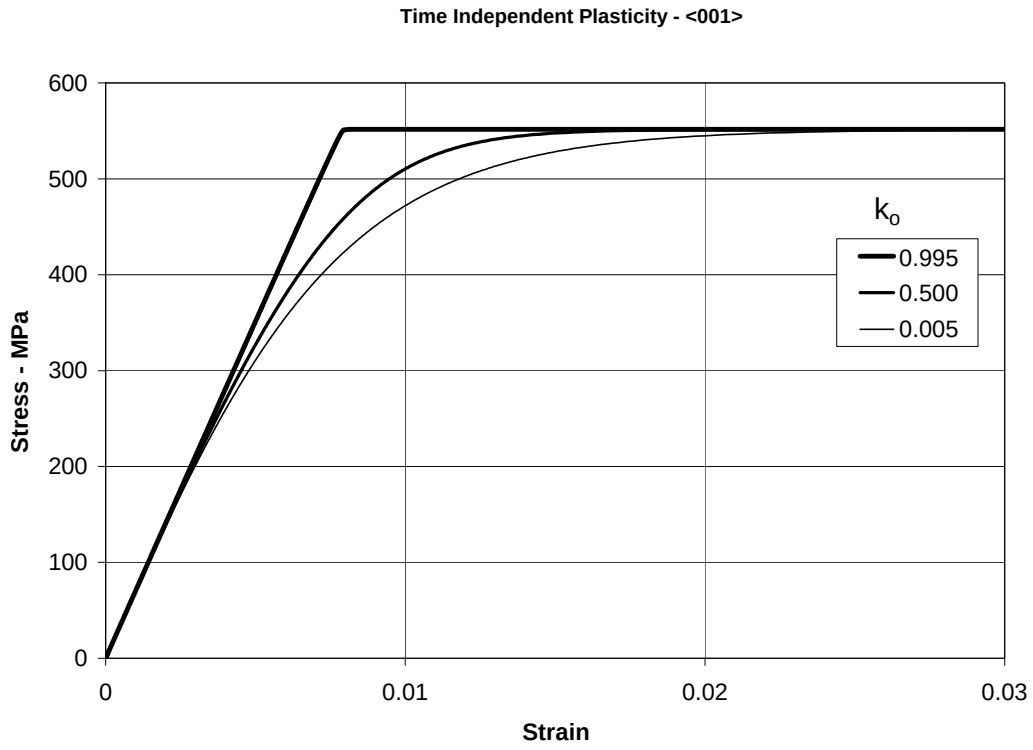

Figure 1. Typical stress-strain curves obtained with rate-independent model with different values of parameter k_0.

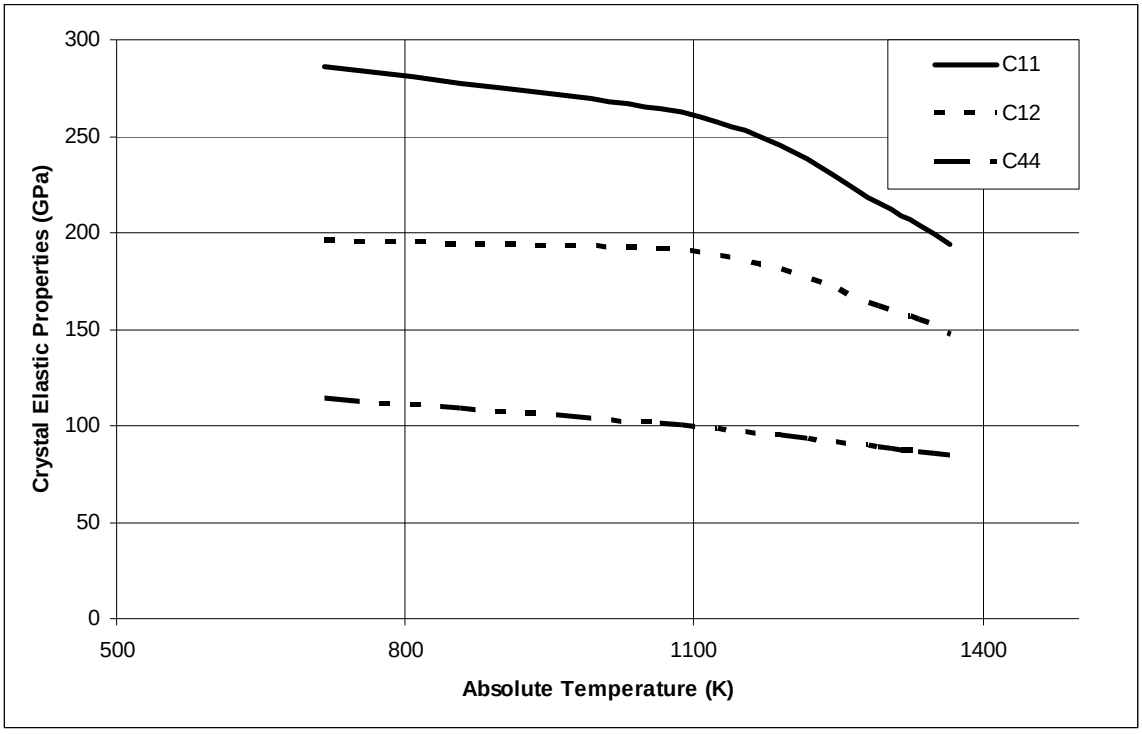

Figure 2. Variation of Elastic Properties with Temperature.

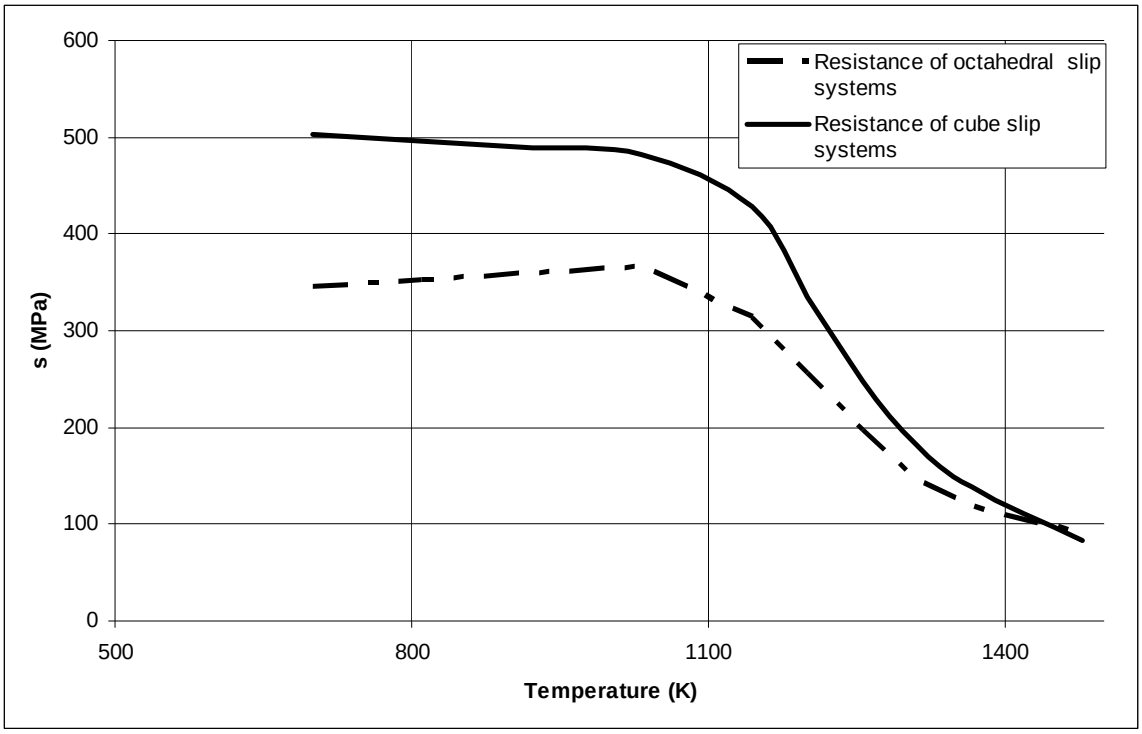

Figure 3. Variation of Initial slip resistances for octahedral and for cube slip systems with Temperature.

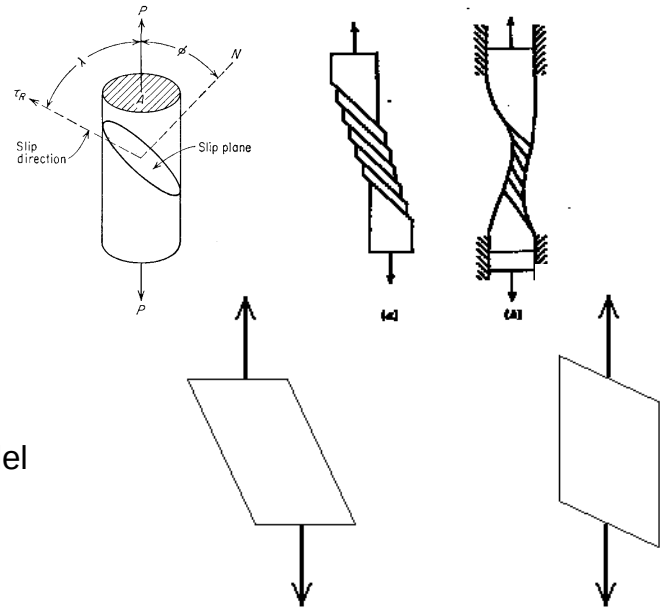

Figure 4. Elements of disturbed lattice without constraint and with stiff constraint (from Dieter 1988) and two types of boundary conditions applied to single elements to simulate simple tension.

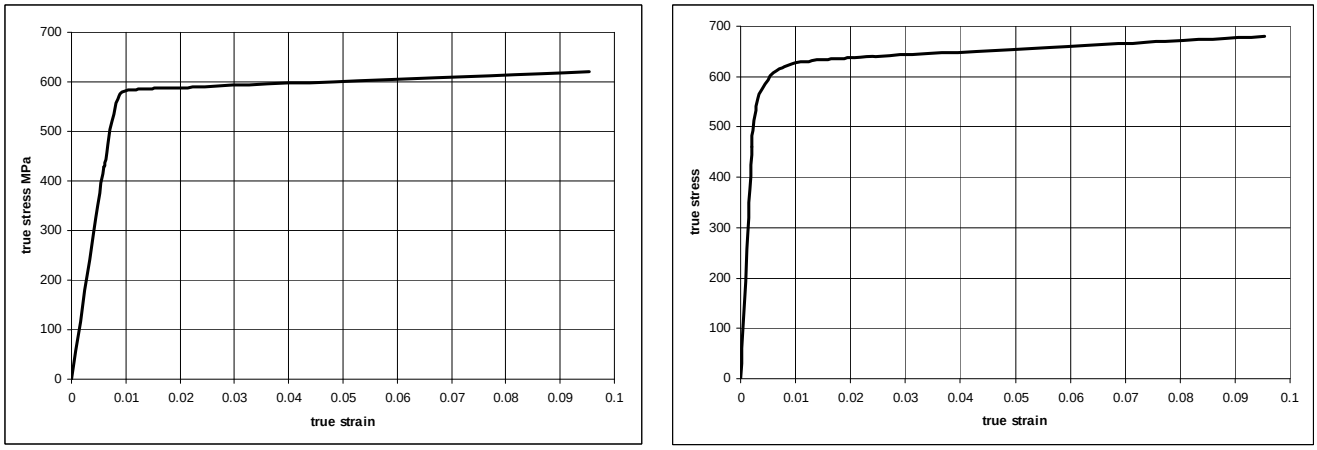

Figure 5. Stress-strain relations for simple tension along (a) <001> and for (b) <111> crystallographic orientation

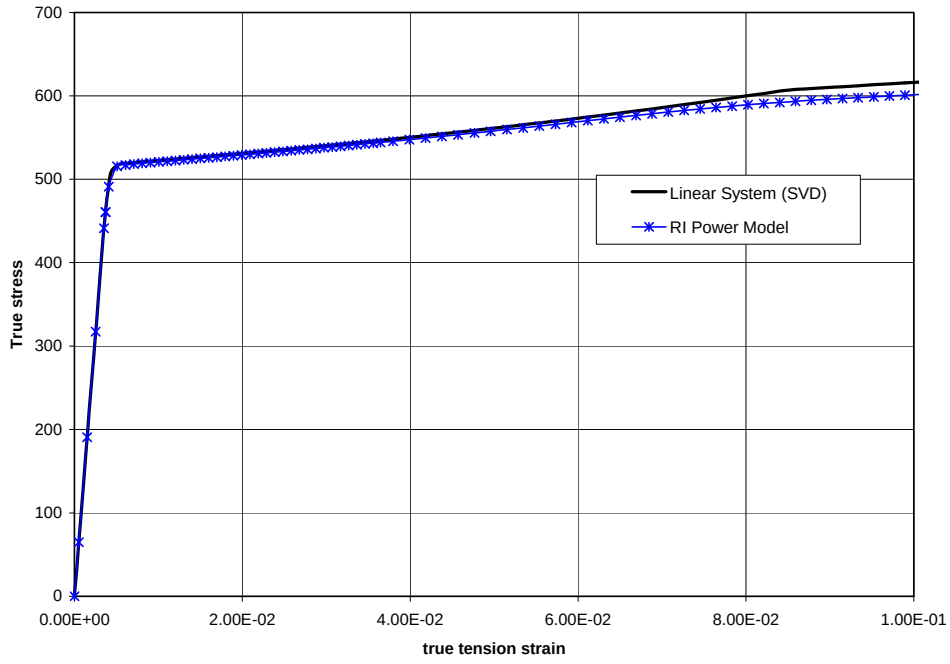

Figure 6. Stress-Strain relations for simple tension along $< \bar{2}36 >$ crystallographic orientation obtained by both reported methods of rate-independent plasticity.

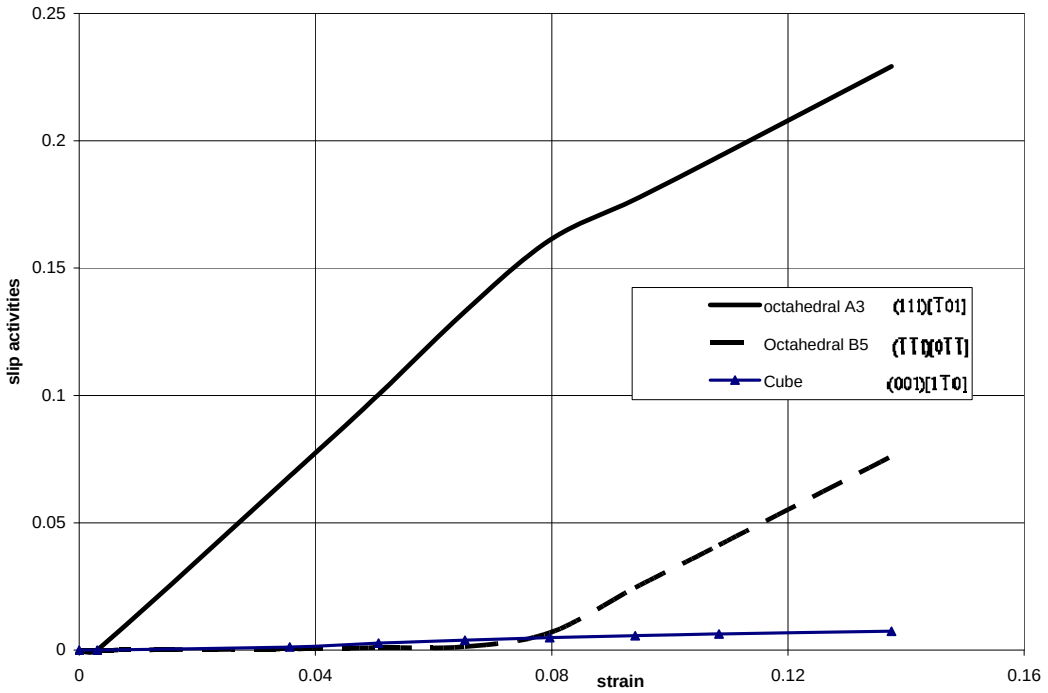

Figure 7. Slip systems activity for simple tension of single crystal PWA 1484 along $< \bar{2}36 >$ crystallographic orientation.

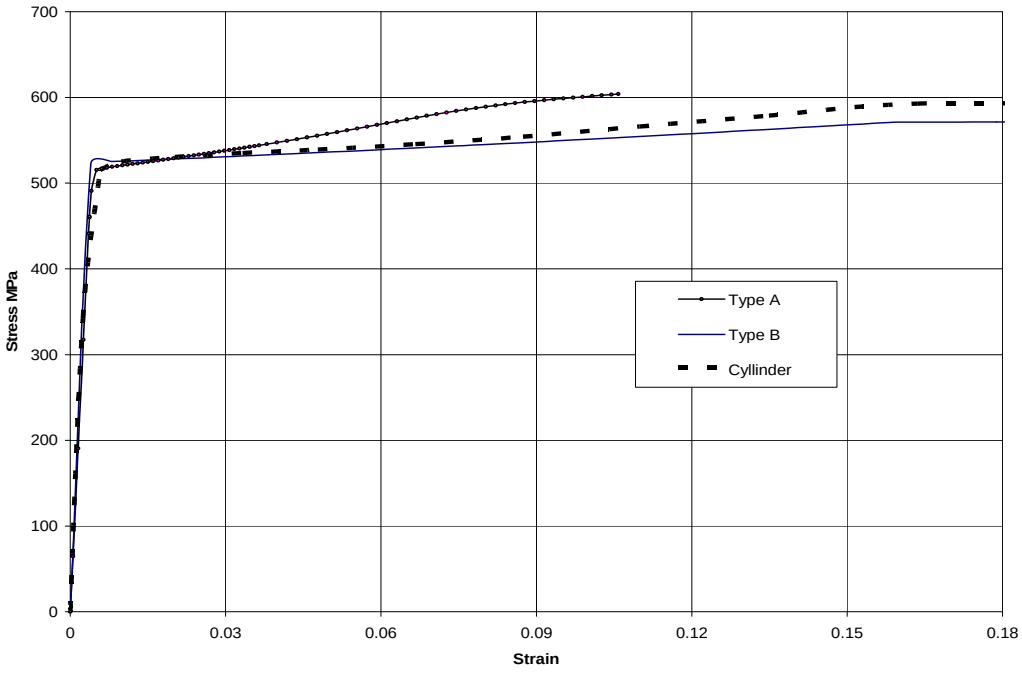

Figure 8. Stress-Strain relations for simple tension along $< \bar{2}36 >$ crystallographic numerically orientation obtained by applying different boundary conditions (single element type A and type B) and for an element in the 3744 –element cylinder model.

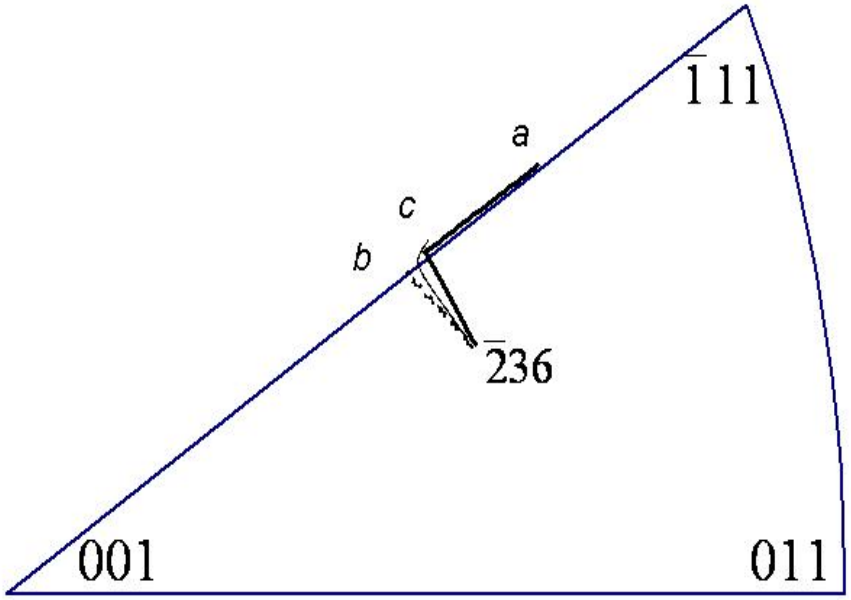

Figure 9. Crystal lattice re-orientation of the single $L1_2$ crystal due to simple tension along $< \bar{2}36 >$ crystallographic axis; (a) Type A boundary conditions, (b) Type B loading conditions, and (c) central element of the cylinder model.

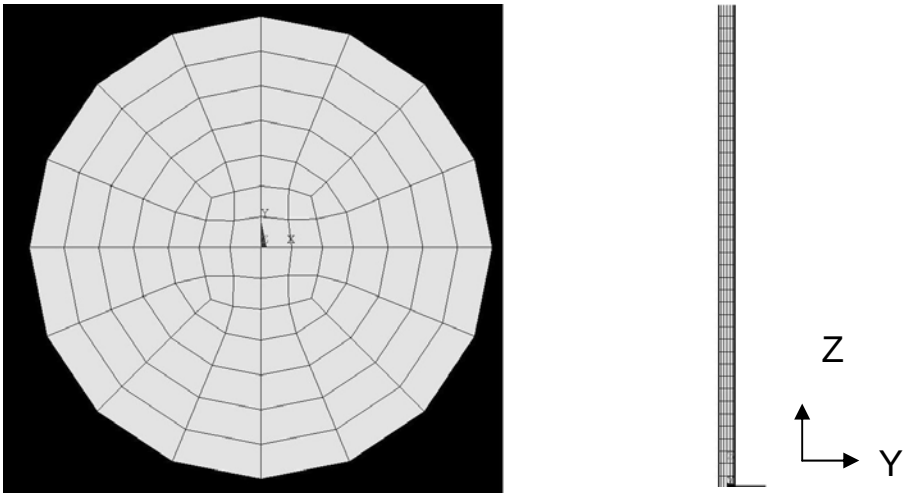

Figure 10. Cylinder FEM used for the simulation of single crystal tensile sample

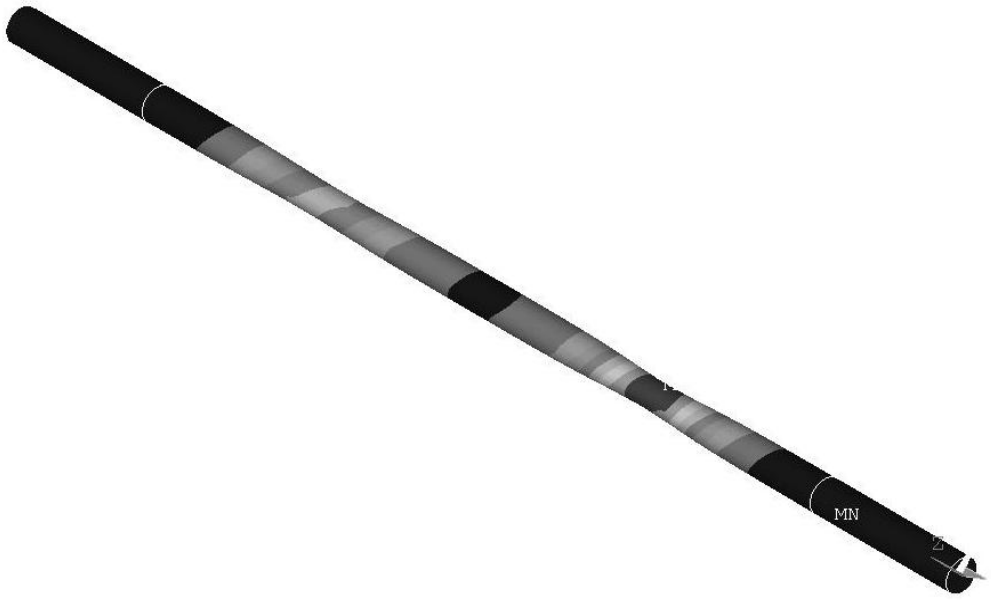

Figure 11. Stereographic view of the necked $< \bar{2}36 >$ single crystal specimen after overall tension to 20%.

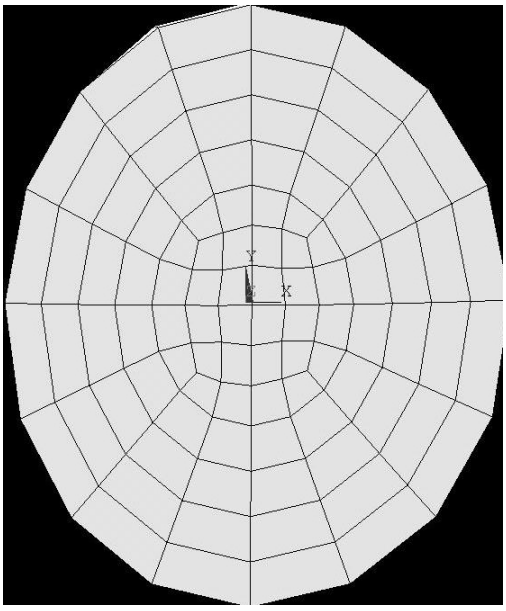

Figure 12. Elliptical cross-section in the necked part of the specimen

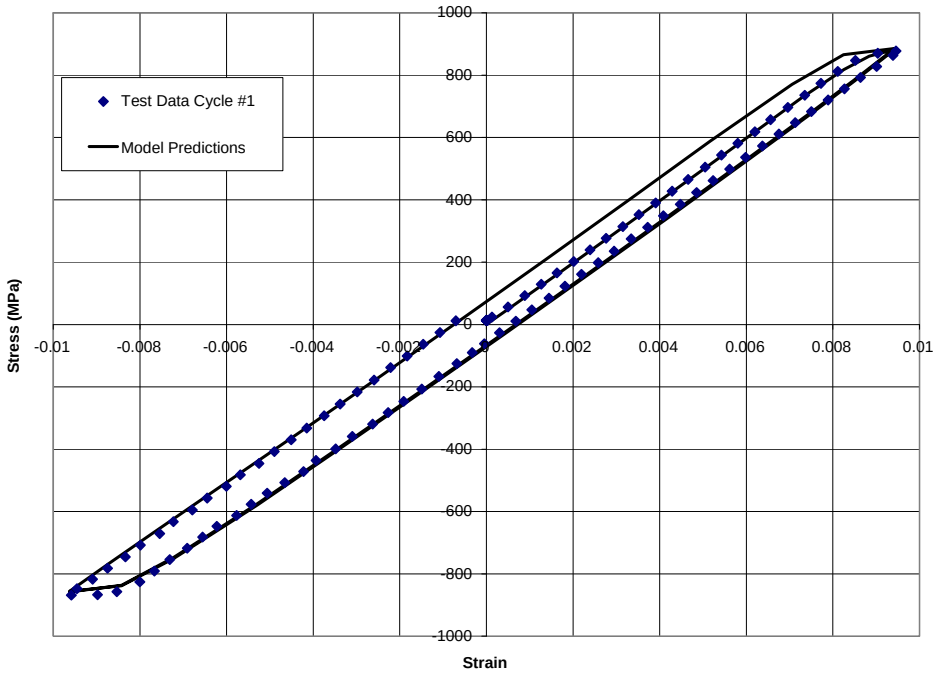
Test Data Cycle #1
Model Predictions
Stress (MPa)
Strain
1000
800
600
400
200
0
-200
-400
-600
-800
-1000
-0.01
-0.008
-0.006
-0.004
-0.002
0
0.002
0.004
0.006
0.008
0.01

(a)

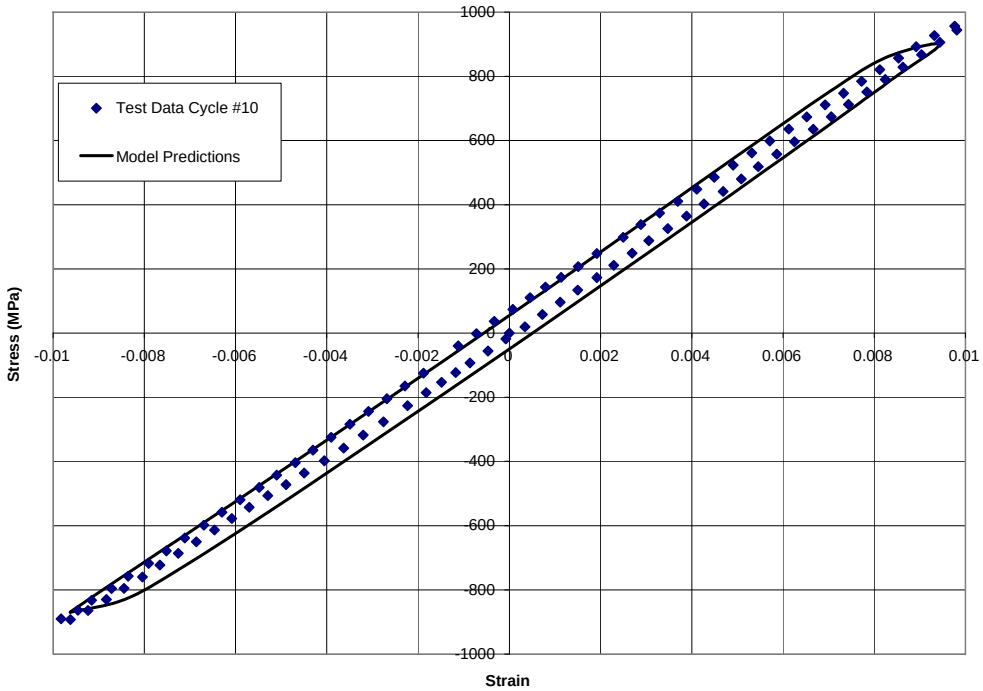
Test Data Cycle #10
Model Predictions
Stress (MPa)
Strain
1000
800
600
400
200
0
-200
-400
-600
-800
-1000
-0.01
-0.008
-0.006
-0.004
-0.002
0
0.002
0.004
0.006
0.008
0.01

(b)

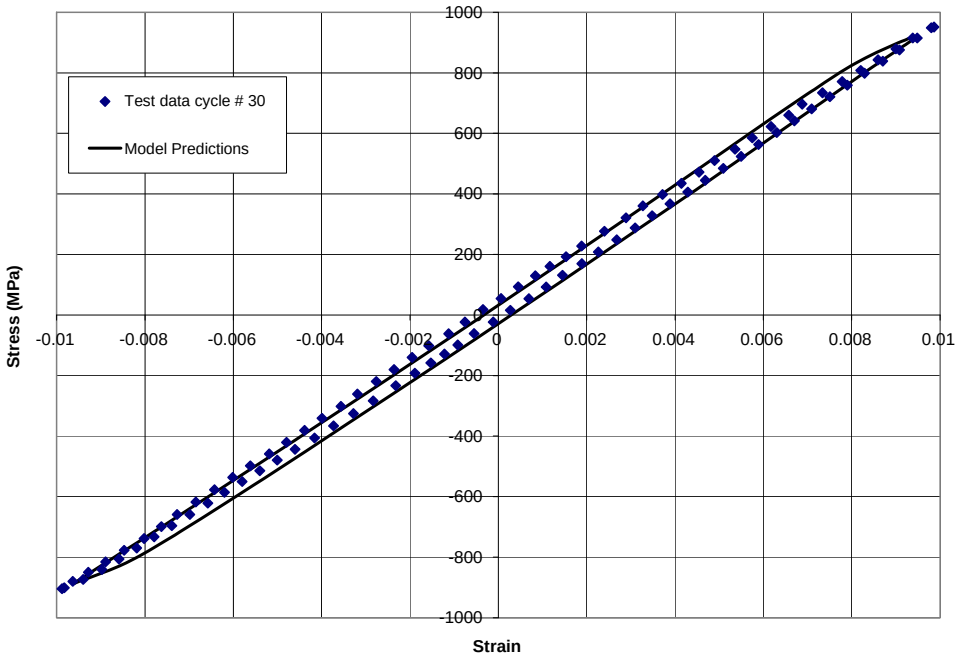

(c)

Figure 13. Predicted stress-strain relations against experimental data for strain-controlled cyclic test up to 1% strain along <001> crystallographic direction at 870 C. Results are shown for the first cycle (a), cycle 10 (b), and cycle 30 (c).

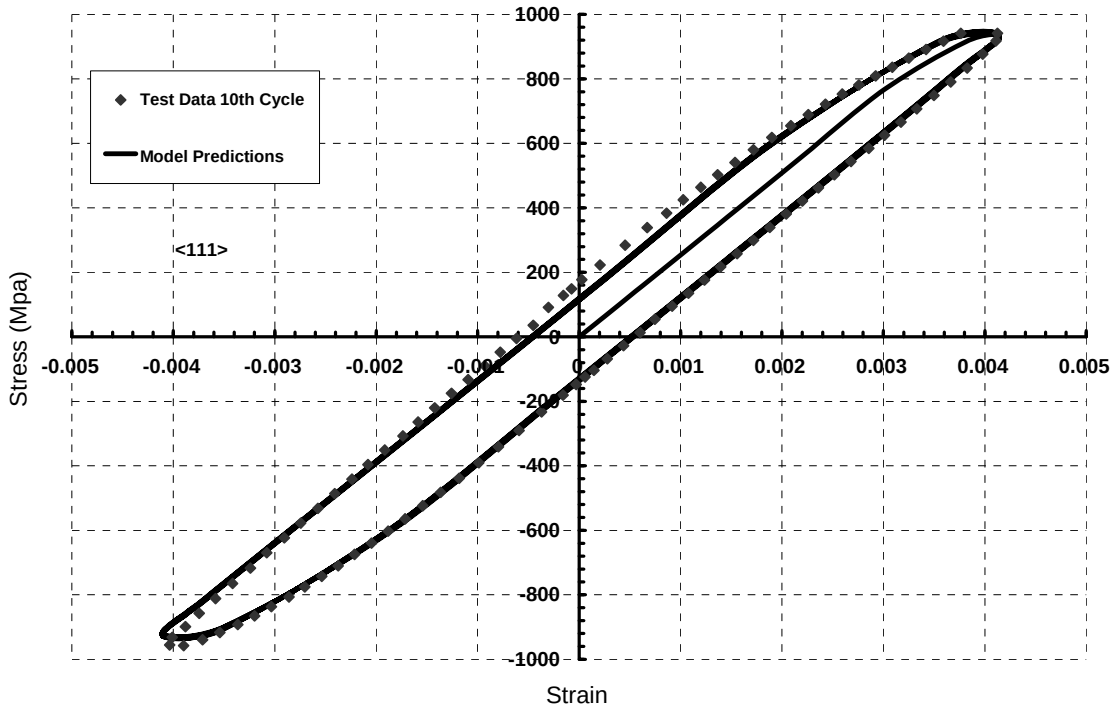

Figure 14. Predicted stress-strain relations against experimental data for strain-controlled cyclic test up to 0.8% strain range along <111> crystallographic direction at 870 C.

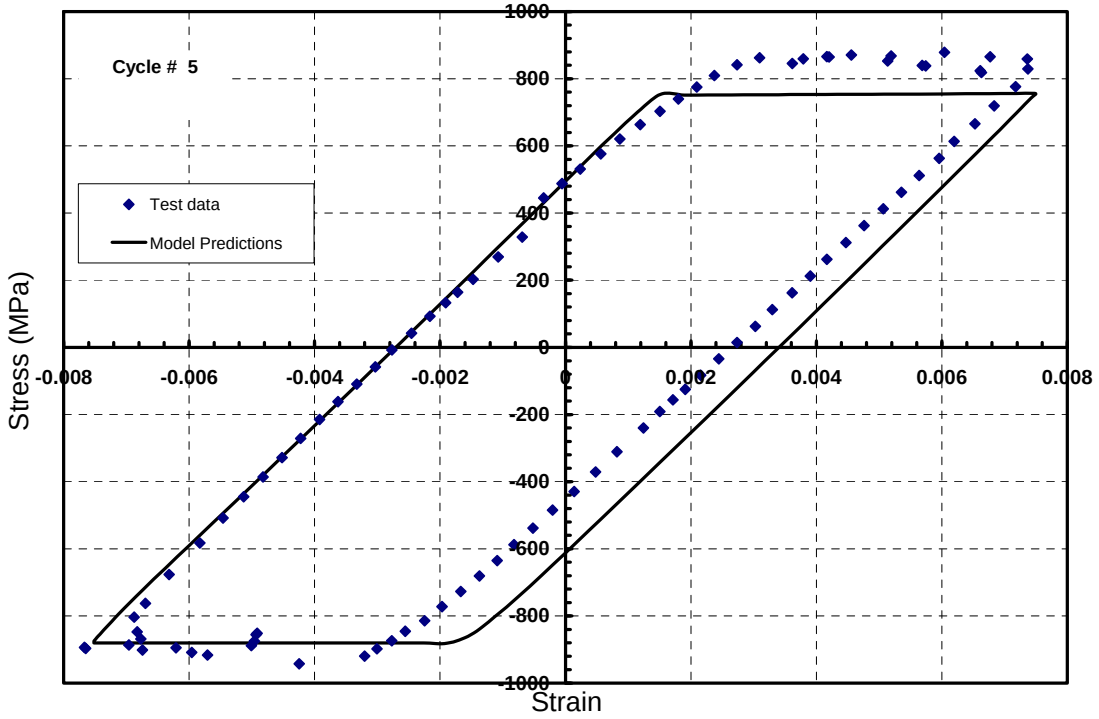

Figure 15. Predicted stress-strain relations against experimental data for strain-controlled cyclic test up to 0.8% strain range along $< \bar{1}23 >$ crystallographic direction at 870 C.